Institution of MECHANICAL ENGINEERS

JOURNAL OF AEROSPACE ENGINEERING

Proceedings of the Institution of Mechanical Engineers
Part G

journals.sagepub.com/home/pig

Volume 231 Issue 13
November 2017
ISSN 0954-4100

Proceedings of the Institution of Mechanical Engineers, Part G: Journal of Aerospace Engineering

Table of Contents: Current Issue

Volume 231, Issue 13, November 2017

Original Articles

Vahid Ghasemzadeh, **Mohammad M Arefi**

First Published August 11, 2016; pp. 2345–2361

Abstract

> Preview

Effects of rotational speed on the leakage behavior, temperature increase, and swirl development of labyrinth seal in a compressor stator well

Gaowen Liu, **Xiaozhi Kong**, **Yuxin Liu**, **Qing Feng**

First Published August 31, 2016; pp. 2362–2374

Abstract

> Preview

Feasibility investigation of large-scale model suspended by cable-driven parallel robot in hypersonic wind tunnel test

Xiaoguang Wang, **Miaojiao Peng**, **Zhenghong Hu**, **Yueshi Chen**, **Qi Lin**

First Published August 8, 2016; pp. 2375–2383

Abstract

> Preview

Airfoil performance degradation by coupling effects of supercooled raindrop icing and heavy rainfall

Zhenlong Wu, **Yihua Cao**

First Published August 30, 2016; pp. 2384–2395

Abstract

> Preview

Airframe/intake–exhaust integration design of flying wing using a multi-bump strategy

Wenbiao Gan, **Zhou Zhou**, **Xiaocui Zhang**

First Published August 21, 2016; pp. 2396–2407

Abstract

> Preview

Flow control for suppression of self-excited rolling oscillation at high angles of attack

Xi Geng, **Zhiwei Shi**, **Keming Cheng**, **Zheng Li**

First Published September 20, 2016; pp. 2408–2422

Abstract

> Preview

Unsteady numerical investigation of two different corrugated airfoils

WH Ho, **TH New**

First Published December 16, 2016; pp. 2423–2437

Abstract

Preview

Vortex flow and lift generation of a non-slender reverse delta wing

T Lee, **LS Ko**

First Published October 12, 2016; pp. 2438–2451

Abstract

Preview

Model-based analysis of boundary layer ingestion effect on lateral-directional aerodynamics using differentiated boundary conditions

Jing Zhang, **Xianfa Zeng**, **Lingyu Yang**

First Published September 14, 2016; pp. 2452–2463

Abstract

Preview

Refined zigzag theory for vibration analysis of viscoelastic functionally graded carbon nanotube reinforced composite microplates integrated with piezoelectric layers

A Ghorbanpour Arani, **M Mosayyebi**, **F Kolahdouzan**, **R Kolahchi**, **M Jamali**

First Published September 14, 2016; pp. 2464–2478

Abstract

Preview

Dynamic soaring of unmanned aerial vehicle within airliner wake vortex in climb regime

Pavel Zikmund, **Jiří Matějů**

First Published September 14, 2016; pp. 2479–2486

Abstract

Preview

Efficiency analysis of moving-magnet linear oscillating motor with dual-resonance for linear electro-hydrostatic actuator

Tianyi Wang, **Zongxia Jiao**, **Liang Yan**

First Published November 25, 2016; pp. 2487–2501

Abstract

Preview

Thermally induced deformation of ultra-large truss support membrane structure

Jie Wang, **Dongxu Li**, **Jianping Jiang**

First Published September 14, 2016; pp. 2502–2512

Abstract

Preview

Original Article

Institution of MECHANICAL ENGINEERS
Journal of AEROSPACE ENGINEERING

Proc IMechE Part G:
J Aerospace Engineering
2017, Vol. 231(13) 2452–2463

DOI: 10.1177/0954410016667148
journals.sagepub.com/home/pig
SAGE

Model-based analysis of boundary layer ingestion effect on lateral-directional aerodynamics using differentiated boundary conditions

Jing Zhang[1], Xianfa Zeng[2] and Lingyu Yang[1]

Abstract

The noteworthy feature of aircraft with distributed propulsion configuration is the integration of a blended-wing-body type airframe and an embedded distributed propulsion system, thus inducing the specific boundary layer ingestion effect. Different boundary layer ingestion effects on the distributed engines may generate asymmetric flow fields on the airframe surface, and then lead to the unique lateral-directional aero-propulsive close coupling. To investigate the lateral-directional aerodynamics influenced by boundary layer ingestion, a new comprehensive computational method based on the differentiated boundary conditions is proposed. This method uses a synthetic three-dimensional computational model including the airframe and multi-engine to analyze the aerodynamic characteristics, and the essential boundary conditions can be extracted from the thermodynamic distributed propulsion system model to represent the different boundary layer ingestion intensities on the left and right engines. Subsequently, detailed model-based analyses of boundary layer ingestion influences on the lateral-directional aerodynamic characteristics are conducted, and the influence regularities under different flight states are revealed. All the results demonstrate that the differentiated boundary layer ingestion intensities on distributed engines can certainly affect the roll and yaw aerodynamic performance of the distributed propulsion configuration aircraft.

Keywords

Boundary layer ingestion, lateral-directional aerodynamics, distributed propulsion configuration, computational fluid dynamics, differentiated boundary conditions

Date received: 14 February 2016; accepted: 30 July 2016

Introduction

Requirements for greener aviation have led to the innovative design of civil aircraft. Distributed propulsion configuration (DPC),[1–6] considered by some to be the most probable trend for commercial airliner, is a new integrated design provided for civil aircraft to effectively improve fuel economy and reduce pollution emission. Compared to the conventional configuration with the tube-and-wing airframe and independently podded engines, the noteworthy feature of DPC is the integration of a blended-wing-body (BWB) type airframe and an embedded distributed propulsion system (DPS), inducing the specific boundary layer ingestion (BLI) effect.[7–11] By ingesting the fuselage boundary layer into the engines, potential benefits in the aircraft efficiency and fuel consumption can be distinctly obtained;[12–15] however, the aerodynamics and propulsion of the DPC aircraft are closely coupled as well. Especially, DPC is composed of multi-engine with individually adjusted control parameters, and may form the different intensities of BLI on the distributed engines. This will generate the asymmetric flow fields on the airframe surface, and then lead to the corresponding unique lateral-directional aerodynamic characteristics. Hence, the lateral-directional aero-propulsive coupling effect becomes a unique feature for this type of aircraft. As the most important characteristic of DPC, the aero-propulsive coupling effect should be thoroughly explored to precisely develop the comprehensive model including flight and propulsion, and ultimately to achieve the integrated flight/propulsion control of the DPC aircraft. In view of this, it is therefore

[1]Science and Technology on Aircraft Control Laboratory, Beijing University of Aeronautics and Astronautics, Beijing, China
[2]Beijing Institute of Control & Electronics Technology, Beijing, China

Corresponding author:
Jing Zhang, Science and Technology on Aircraft Control Laboratory, Beijing University of Aeronautics and Astronautics, New Main Building E602, No. 37, Xueyuan Road, Haidian District, Beijing 100191, China.
Email: zhangjing2013@buaa.edu.cn

necessary to systematically study the lateral-directional aero-propulsive close coupling influenced by BLI.

Current research on the aero-propulsive coupling effect usually focuses on the longitudinal aerodynamic characteristics influenced by BLI. Lugo et al.[16] investigated the effects of BLI on the aerodynamics of a transonic wing using a two-dimensional (2D) computational model of a transonic airfoil with BLI propulsion system. A preliminary parametrical analysis of a supercritical airfoil with BLI was conducted, and effects of the mass flow ratio, Mach number, angle of attack, and geometrical parameters on the longitudinal aerodynamic performance of the aircraft wing were analyzed numerically. Computational results demonstrated that the high mass flow ratio enhanced the acceleration on the upper surface of the airfoil, thus had a beneficial effect on the aerodynamic lift. Kerho[17] conducted a computational investigation into the aero-propulsive coupling effects of a set of boundary layer ingesting fans mounted near the trailing edge of a wing. A computational model of a 5-fan turboelectric distributed propulsion geometry based on a NACA 64_3-618 section was developed to study the aerodynamic/propulsive coupling effects and, subsequently, the effects of different fan thrust angels and fan thrust levels were investigated. The results from the investigation showed that varying the fan thrust angle or the fan thrust level would significantly affect the sectional lift, drag, and pitching moment. Wick et al.[18] selected three candidate distributed propulsion configurations, including the upper trailing edge, the lower trailing edge, and the embedded concepts to integrate with a representative conventional aircraft, and a baseline assessment of their aerodynamic performance was performed by computational fluid dynamics (CFD). The simplified 2D study and detailed 3D study were carried out in sequence, and the performance was compared with conventional under wing engine installations of equivalent fan propulsive areas. To model the BLI effects, the modified CFD boundary condition was also calculated that enabled the simulation of fans running at constant power settings. This research revealed that the development of an embedded configuration had an 8% improved longitudinal aerodynamic efficiency at transonic flight conditions. Kang et al.[19] conducted a preliminary research on the aerodynamic lift and drag characteristics with different BLI effects. Based on a simplified 2D sectional model of the DPC aircraft, the detailed numerical analysis of BLI influences on the aerodynamics was carried out. Computational results indicated that the BLI effect had extraordinary potential to improve the aerodynamic lift and lift-to-drag ratio characteristics.

In all, the existing studies mostly concentrate on the longitudinal aerodynamic performance of the DPC aircraft; however, the literature on the lateral-directional aero-propulsive coupling effect has still rarely appeared. Aiming at this problem, the unique lateral-directional aerodynamic characteristics due to different BLI effects is primarily investigated in this article. First, a general comprehensive computational method based on the differentiated boundary conditions is proposed. As DPC is still in the conceptual design phase, the most feasible approach is to analyze the aero-propulsive coupling by CFD computations. In view of this, this article presents a model-based 3D computational method in which the essential boundary conditions are extracted from the DPS thermodynamic model to represent the different BLI intensities on the left and right engines. Subsequently, to validate the effectiveness of this proposed method, model-based CFD computational analyses of BLI influences on the lateral-directional aerodynamic performance are carried out for a specific DPC aircraft. And then the valuable regularities of computation results under different BLI effects and flight states are explored.

The article is organized as follows. The description of the 3D computational method based on boundary conditions is presented first. This section is then followed by the determination of differentiated boundary conditions for distributed engines. After which, BLI influences on the lateral-directional aerodynamic characteristics for a specific DPC aircraft at different flight states are investigated by CFD. Lastly, conclusions are stated in the final section.

Description of the 3D computational method based on boundary conditions

To accurately investigate the BLI effect on the lateral-directional aerodynamics, a comprehensive 3D computational method based on the boundary conditions is proposed in this section. This method consists of three main steps. The first step is to build a synthetic 3D computational model, which includes the blended-wing-body airframe and the embedded distributed propulsion system. The multiple distributed engines have separate control parameters, in order to realize the differentiated BLI on the left and right engines respectively. The second step is to acquire the differentiated boundary conditions based on the thermodynamic DPS model. Boundary conditions at engine inlet and nozzle exhaust outlet are provided by the actual response surface parameters of the DPS model. Synthesizing the 3D computational model and differentiated boundary conditions, CFD computations can be conducted in the third step. By fully utilizing the obtained boundary conditions, the flow field with BLI is simulated, and then the roll and yaw moment coefficients can be reliably calculated under different BLI effects.

SAX-40 is selected as the object to further describe the detailed computational process. SAX-40 is a prominent achievement of the Silent Aircraft Initiative program conducted by Cambridge University and MIT,[4,5] which utilizes a representative 3-engine configuration to achieve the benefits of distributed propulsion.

Step 1: According to SAX-40's shape construction, a 3D blended-wing-body model is built initially, and then three distributed engines are embedded in the upper surface trailing-edge ingesting the boundary layer. The synthetic 3D computational model in CFD is illustrated in Figure 1.

The control parameters of SAX-40's three distributed engines can be adjusted individually, such as the pressure ratio of the fans π_k, and the nozzle exit area A_8. Each control set (π_k,A_8) directly corresponds to a specific boundary layer ingestion intensity η_{BLI}, and corresponds to the specific boundary conditions as well. Boundary conditions include engine's inflow parameters (T_1,P_1,q_m) and outflow parameters (T_8,P_8,V_8). T,P,V,q_m represent respectively the static temperature, the static pressure, the velocity, and the air flow rate. Subscripts "1" and "8" refer to engine inlet and nozzle exhaust outlet, respectively.

Step 2: According to the current flight altitude h and Mach number M, the reference aerodynamic parameters are obtained by CFD with a 3D blended-wing-body model. Then the flight/propulsion matching analysis with the DPS model is conducted to determine the thrust range, as well as the corresponding range of DPS control sets (π_k,A_8). After that, the feasible differentiated boundary conditions are determined and set on the left and right engines separately, in order to simulate different BLIs on the distributed engines of the DPC aircraft. For the left engine, its inflow and outflow parameters are set as (T_{1_left}, P_{1_left}, q_{m_left}), (T_{8_left}, P_{8_left}, V_{8_left}), with the corresponding boundary layer ingestion intensity η_{BLI_left}. Similarly, for the right engine, the boundary conditions are set as (T_{1_right}, P_{1_right}, q_{m_right}), (T_{8_right}, P_{8_right}, V_{8_right}), with the corresponding ingestion intensity η_{BLI_right}. By changing the engine's inlet and outlet feature parameters, the different BLI effects on the left and right engines can be represented and the impact to the lateral-directional aerodynamics can be analyzed numerically. The differentiated boundary conditions can be provided by the response surface parameters of the thermodynamic DPS model, which is described particularly in the subsequent section.

Step 3: Based on the 3D computational model and differentiated boundary conditions, the CFD analyses are carried out subsequently. By fully using the differentiated boundary conditions, such as (T_{1_left}, P_{1_left}, q_{m_left}), (T_{8_left}, P_{8_left}, V_{8_left}), (T_{1_right}, P_{1_right}, q_{m_right}), (T_{8_right}, P_{8_right}, V_{8_right}), computational fluid dynamics simulations proceed. The flow fields around the airframe and the embedded distributed engines are obtained, and then the lateral-directional aerodynamic characteristics, including the roll and yaw moment coefficients, can be numerically calculated under differentiated BLI effects.

As mentioned above, the comprehensive 3D computational method is gathered and illustrated in Figure 2.

Determination of differentiated boundary conditions

The differentiated boundary conditions are extracted from SAX-40's distributed engine model. SAX-40 utilizes a 3-engine configuration as shown in Figure 1, and each engine has a single core with one low-pressure turbine to drive three fans. A transmission system is used to divide and transmit the required power from the turbine into the distributed fans.[20] The components of each engine include the inlet, distributed fans, the core-engine compressor, the burner, the turbine, and the variable exhaust nozzle. The layout of each engine is illustrated in Figure 3.

In which, "∞" represents the region in the undisturbed airflow far ahead, "1" represents the entrance

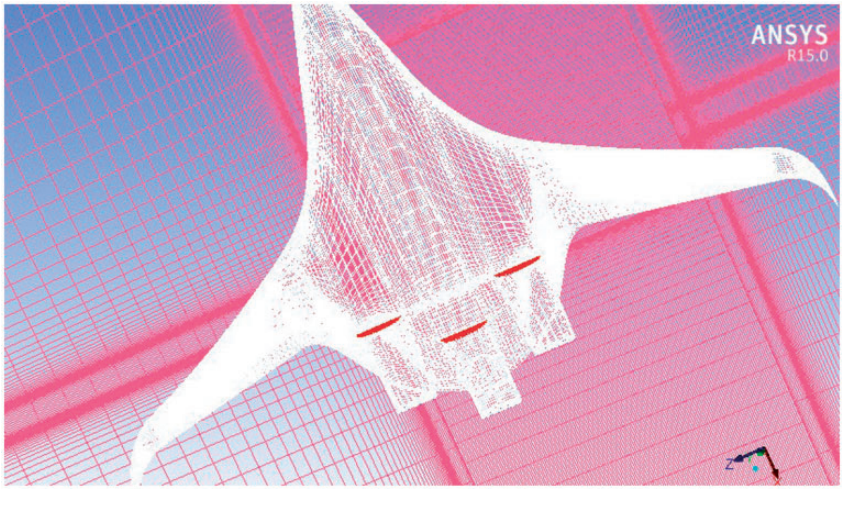

Figure 1. 3D computational model.

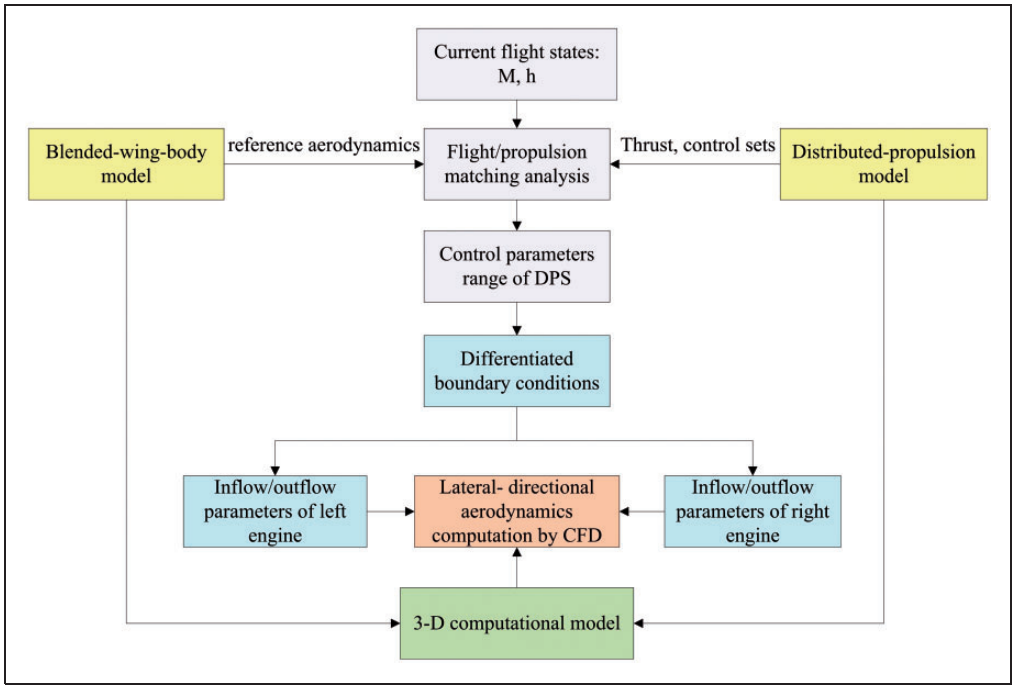

Figure 2. 3D computational method for lateral-directional aerodynamics analysis.

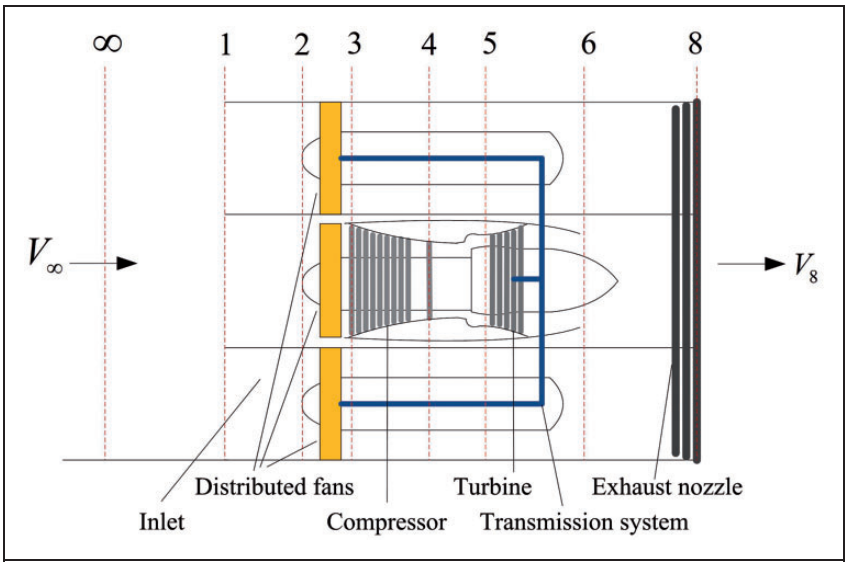

Figure 3. Layout of each engine.

of the inlet, "2" and "3" represent the entrance and exit of distributed fans, respectively, "4" represents the exit of the core-engine compressor, "5" and "6" represent the front and rear sections of the turbine, and "8" represents the exit of the exhaust nozzle.

Boundary conditions, i.e. the inflow and outflow parameters are determined by the inherent characteristics and the thermodynamic process of all components, described as follows.

Supposing the flight altitude h and Mach number M, the static pressure, temperature, and the free-stream velocity (P_0, T_0, V_∞) of the undisturbed airflow can be obtained.[21]

Inlet: According to P_0, T_0, the entrance parameters of the inlet can be calculated by

$$P_1^* = P_0\left(1 + \frac{\gamma - 1}{2} M^2\right)^{\frac{\gamma}{\gamma - 1}} \tag{1}$$

$$T_1^* = T_0\left(1 + \frac{\gamma - 1}{2} M^2\right) \tag{2}$$

where γ is the specific heat ratio, P^*, T^* refer to the total pressure and temperature in this article, and numbers in the subscripts represent the corresponding stations in Figure 3.

The total pressure recovery coefficient σ_i is selected to represent the loss of total pressure in the inlet, and consequently the characteristic component equations are expressed as

$$P_2^* = \sigma_i * P_1^*,\ T_2^* = T_1^*$$

Distributed fans and core-engine compressor: Distributed fans include one core-engine fan and two propulsor fans on each side. The air flow in the distributed fans and core-engine compressor is approximately considered as the isentropic process. Then the thermodynamic equations of all fans and compressor can be expressed as

$$P_{3\_ex}^* = \pi_{k\_ex} * P_2^*, \quad P_{3\_in}^* = \pi_{k\_in} * P_2^*$$

$$T_{3\_ex}^* = \left(1 + \left(\pi_{k\_ex}^{\frac{\gamma-1}{\gamma}} - 1\right)\frac{1}{\eta_{k\_ex}}\right) * T_2^*,$$
$$T_{3\_in}^* = \left(1 + \left(\pi_{k\_in}^{\frac{\gamma-1}{\gamma}} - 1\right)\frac{1}{\eta_{k\_in}}\right) * T_2^*,$$

$$P_4^* = \pi_c * P_{3\_in}^*,$$

$$T_4^* = \left(1 + \left(\pi_c^{\frac{\gamma-1}{\gamma}} - 1\right)\frac{1}{\eta_c}\right) * T_{3\_in}^*$$

where π_k,η_k are the fan pressure ratio and efficiency, π_c,η_c are the core-engine compressor pressure ratio and efficiency, respectively. Subscripts *ex*,*in* refer to the external propulsor fans and the internal core-engine fan, respectively.

Burner: After the core-engine compressor, the high-pressure air enters into the burner to fully mix with fuel flow. Two important parameters are the total pressure recovery coefficient σ_b and the burn efficiency η_b.

Assuming the fuel flow is q_{mf}, and thus the burner exit mass flow is $q_{m5} = q_{mf} + q_m$ with the corresponding fuel-to-air ratio being $f = q_{mf}/q_m$. According to the enthalpy function $H_e = g(T^*,f)$, the enthalpy value of the burner entrance H_4 can be determined as $H_4 = g(T_4^*,f)$. Then the burner exit enthalpy value H_5 is calculated as follows

$$H_5 = \frac{q_m * H_4 + q_{mf} * H_u\eta_b}{q_{m5}}$$

where H_u is the fuel heat value. Correspondingly the burner exit temperature T_5^* is obtained.

Based on the characteristic parameter σ_b, the total pressure at the burner exit is also calculated as

$$P_5^* = \sigma_b * P_4^*$$

Turbine: The purpose of the turbine is to transmit the required power to distributed fans. On the basis of the turbine entrance pressure and temperature (P_5^*,T_5^*), the turbine exit parameters can be computed by

$$P_6^* = \frac{P_5^*}{\pi_g},$$

$$T_6^* = T_5^*\left[1 - \left(1 - \frac{1}{\pi_g^{\frac{\gamma-1}{\gamma}}}\right)\eta_g\right]$$

where π_g,η_g are the turbine pressure ratio and efficiency, respectively.

Nozzle: The air flow in the nozzles can be approximately regarded as the isentropic process. Then for the internal and external nozzles, the total pressure and temperature at the exit are obtained as follows

$$P_8^* = \sigma_n * P_n^*, \quad T_8^* = T_n^*,$$

$$P_n^* = \begin{cases} P_6^* & \text{for internal} \\ P_{3\_ex}^* & \text{for external} \end{cases},$$
$$T_n^* = \begin{cases} T_6^* & \text{for internal} \\ T_{3\_ex}^* & \text{for external} \end{cases}$$

where σ_n represents the pressure loss in the nozzle. P_n^*,T_n^* are the total pressure and temperature at the entrance of the nozzle.

The compressed air at the nozzle exit should be checked whether it fully expands, and the corresponding expressions satisfy

$$\begin{cases} P_8 = \frac{P_n^*}{\beta_{cr}} & \frac{P_n^*}{P_0} > \beta_{cr} \\ P_8 = P_0 & \frac{P_n^*}{P_0} < \beta_{cr} \end{cases}$$

where P_8 refers to the static pressure of the nozzle exit, β_{cr} is the critical pressure ratio, and $\beta_{cr} = (\frac{2}{\gamma+1})^{\frac{\gamma-1}{\gamma}}$.

Then according to the relationships between the total pressure P_8^* and the static pressure P_8, the total

Table 1. Differentiated boundary conditions.

		Left engine $\eta_{BLI\_left} = 0.97$	Right engine $\eta_{BLI\_right} = 1.05$
Engine inflow parameters	T_1 (K)	224.6	219.9
	P_1 (Pa)	27,036	25,129
	q_m (kg/s)	431.3	469.8
Engine outflow parameters	T_8 (K)	227	227
	P_8 (Pa)	26,436	26,436
	V_8 (m/s)	265.9	277.8

temperature T_8^* and the static temperature T_8

$$\frac{P_8^*}{P_8} = \left(1 + \frac{\gamma - 1}{2} M_8^2\right)^{\frac{\gamma}{\gamma - 1}} \tag{3}$$

$$\frac{T_8^*}{T_8} = 1 + \frac{\gamma - 1}{2} M_8^2 \tag{4}$$

Mach number at the nozzle exit M_8 and the corresponding static temperature T_8 can be determined.

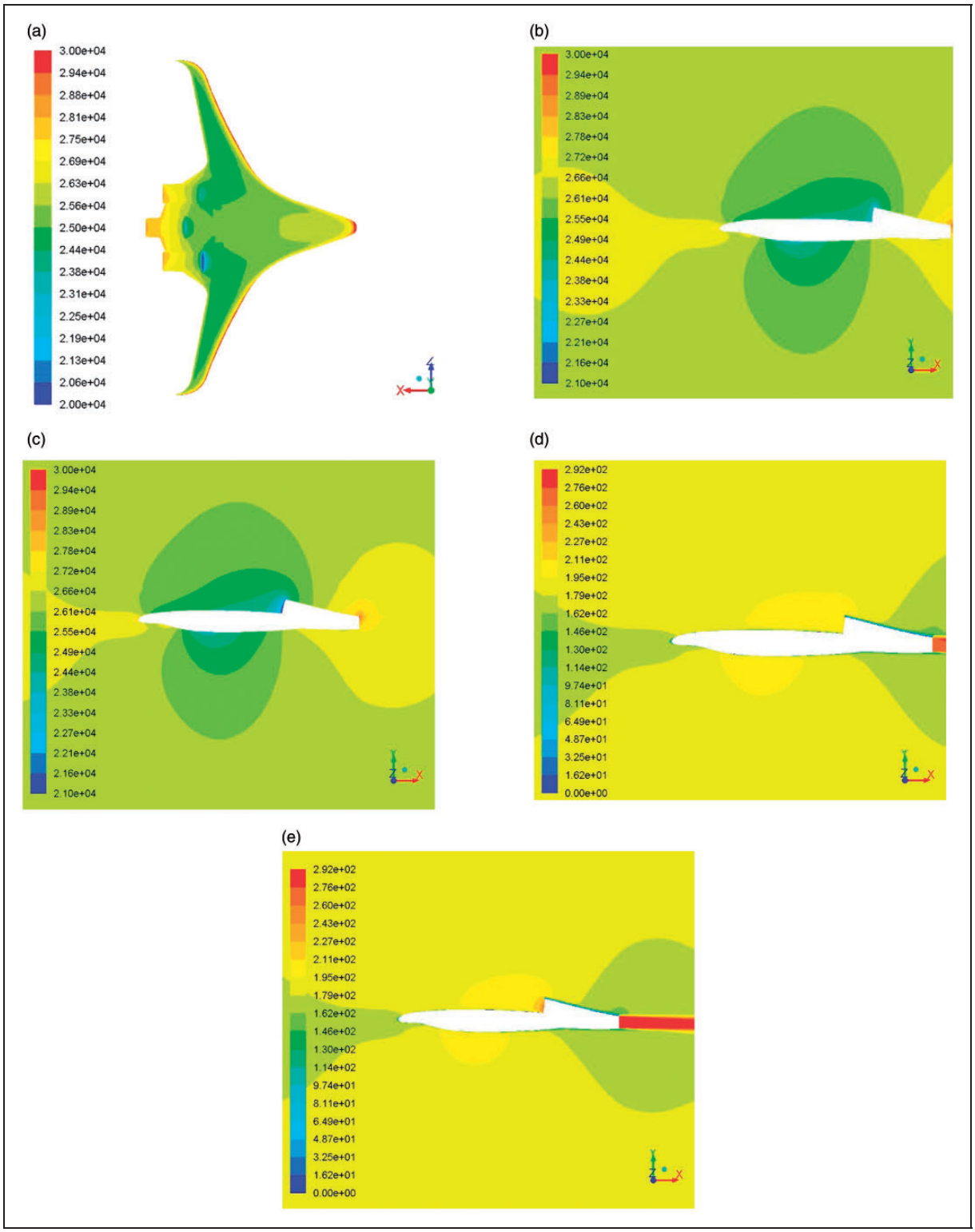

Figure 4. Velocity and pressure plots of $\eta_{BLI\_left} = 0.97$ and $\eta_{BLI\_right} = 1.05$: (a) pressure plot (Pa), $\eta_{BLI\_left} = 0.97$,$\eta_{BLI\_right} = 1.05$; (b) sectional pressure plot on left engine (Pa); (c) sectional pressure plot on right engine (Pa); (d) sectional velocity plot on left engine (m/s); (e) sectional velocity plot on right engine (m/s).

Subsequently, the nozzle exit velocity V_8 is obtained as

$$V_8 = M_8 * \sqrt{\gamma R T_8}$$

where R is the gas constant. And with this, the outflow parameters (T_8, P_8, V_8) are acquired.

The air mass flow rate q_m can be expressed as

$$q_m = K \frac{P_i^* * A_i * q(\lambda_i)}{\sqrt{T_i^*}}$$

where K is the flow coefficient, A is the cross-sectional area of the engine's components. $q(\lambda_i)$ refers to the flow function, which is defined as

$$q(\lambda_i) = \left(\frac{\gamma+1}{2}\right)^{\frac{1}{\gamma-1}} \lambda_i \left(1 - \frac{\gamma-1}{\gamma+1}\lambda_i^2\right)^{\frac{1}{\gamma-1}} \quad (5)$$

in which λ_i is the velocity coefficient related to Mach number.

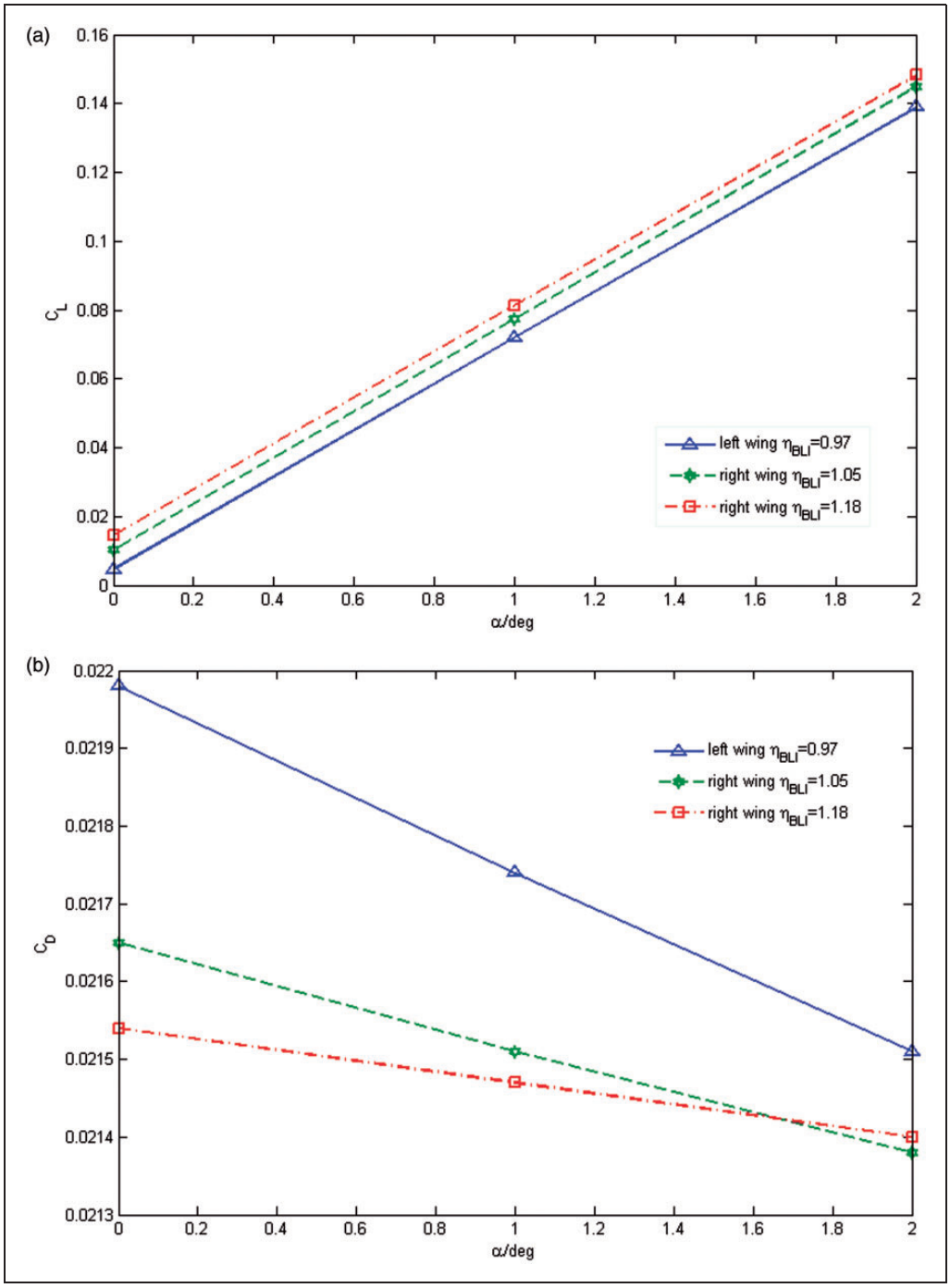

Figure 5. (a) Lift and (b) drag coefficients.

Therefore, the flow function $q(\lambda_1)$at the entrance of the engine inlet satisfies

$$q(\lambda_1) = \frac{A_8 P_8^* \sqrt{T_1^*}}{A_1 P_1^* \sqrt{T_8^*}} q(\lambda_8)$$

Correspondingly, in accordance with equation (5), the velocity coefficient and Mach number at the engine inlet (λ_1, M_1) are obtained.

Similar to equations (3) and (4), the static pressure P_1 and the static temperature T_1 at the engine inlet are calculated by

$$\frac{P_1^*}{P_1} = \left(1 + \frac{\gamma - 1}{2} M_1^2\right)^{\frac{\gamma}{\gamma - 1}}$$

$$\frac{T_1^*}{T_1} = 1 + \frac{\gamma - 1}{2} M_1^2$$

As above, all the boundary conditions including engine's inflow parameters (T_1, P_1, q_m) and outflow parameters (T_8, P_8, V_8) are determined.

For the left and right engines, the control parameters are set as $(\pi_{k\_left}, A_{8\_left})$, $(\pi_{k\_right}, A_{8\_right})$, respectively. Then, the corresponding differentiated boundary conditions $(T_{1\_left}, P_{1\_left}, q_{m\_left})$, $(T_{8\_left}, P_{8\_left}, V_{8\_left})$, and $(T_{1\_right}, P_{1\_right}, q_{m\_right})$, $(T_{8\_right}, P_{8\_right}, V_{8\_right})$ can be separately determined by the calculation process mentioned above. And different BLI intensities η_{BLI_left}, η_{BLI_right} are obtained as

$$\eta_{BLI\_left} = \frac{q(\lambda_{1\_left})}{q(\lambda_\infty)}, \quad \eta_{BLI\_right} = \frac{q(\lambda_{1\_right})}{q(\lambda_\infty)}$$

where λ_∞ is the velocity coefficient of the undisturbed airflow.

Preliminary analysis of BLI effect on lateral-directional aerodynamics

Based on the 3D computational method with differentiated boundary conditions, the direct influences of BLI on the lateral-directional aerodynamic characteristics are investigated systematically in this section. For the conceptual DPC commercial airliner, the cruise Mach range is approximately from Mach number 0.6 to 0.8. Dangelo[1] and Hileman et al.[4] indicate that the cruise speed of the latest generation SAX-40 is designed as $Ma = 0.8$, and the conceptual baseline airliner B-20 is designed to cruise at $Ma = 0.6$. Besides, the CFD computations for the typical conceptual DPC aircraft are conducted for flight Mach numbers ranging from 0.5 to 0.85.[4,6] In addition, the usual cruising altitude range is mainly 8000–12,000 m for most civil airliners. On the basis of the above analysis, two typical flight states $h = 10{,}000$ m, $Ma = 0.6$ and $h = 10{,}000$ m, $Ma = 0.8$ are selected to conduct the preliminary research on the aerodynamic characteristics influenced by BLI.

First, the analysis of the lateral-directional aerodynamic characteristics influenced by BLI is conducted under the typical flight state $h = 10{,}000$ m, $Ma = 0.6$. The differentiated boundary conditions including engine's inflow and outflow parameters for different BLI intensities $\eta_{BLI\_left} = 0.97$, $\eta_{BLI\_right} = 1.05$ are illustrated in Table 1. Figure 4 shows the velocity and pressure plots of the DPC aircraft with the above differentiated BLI intensities.

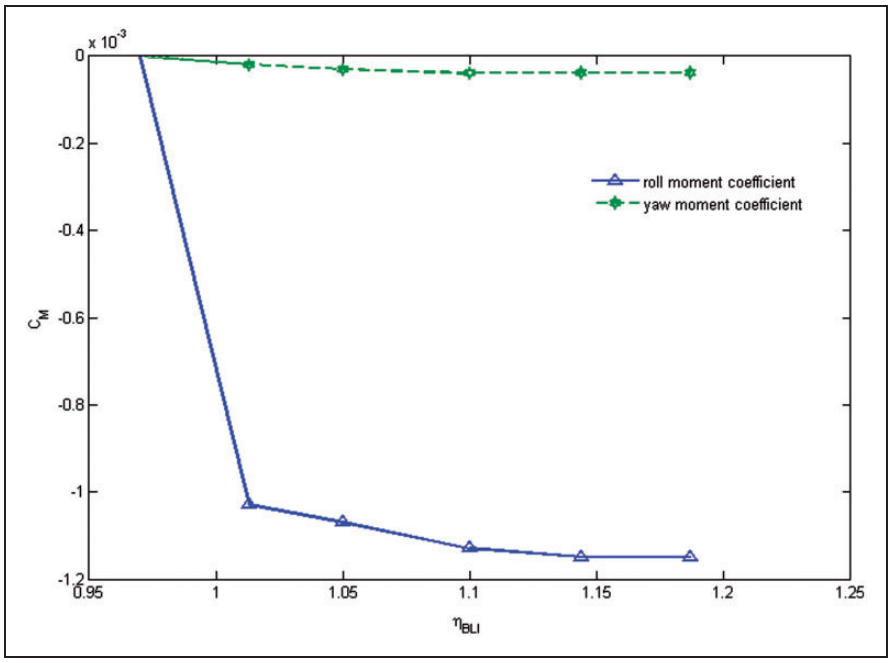

Figure 6. Roll and yaw moment coefficients.

As can be seen, the asymmetric velocity and pressure characteristics appear with the differentiated BLI intensities $\eta_{BLI\_left} = 0.97$, $\eta_{BLI\_right} = 1.05$. Compared to the plots of the left and right engines, it can be easily seen that the flow velocity on the upper surface of airfoil is obviously raised with the larger BLI intensity $\eta_{BLI\_right} = 1.05$ and, in consequence, the static pressure on the upper surface decreases apparently, particularly near the inlet of the right engine. That is, BLI has a direct effect on the velocity and pressure distribution of the DPC aircraft. As a result of the asymmetric velocity and pressure characteristics, the lateral-directional aerodynamics including roll and yaw moments are generated.

Then the influences of BLI on the aerodynamic coefficients are investigated. The lift and drag coefficients C_L,C_D with different BLI intensities $\eta_{BLI\_left} = 0.97$ and $\eta_{BLI\_right} = 1.05$, $\eta_{BLI\_right} = 1.18$ on the

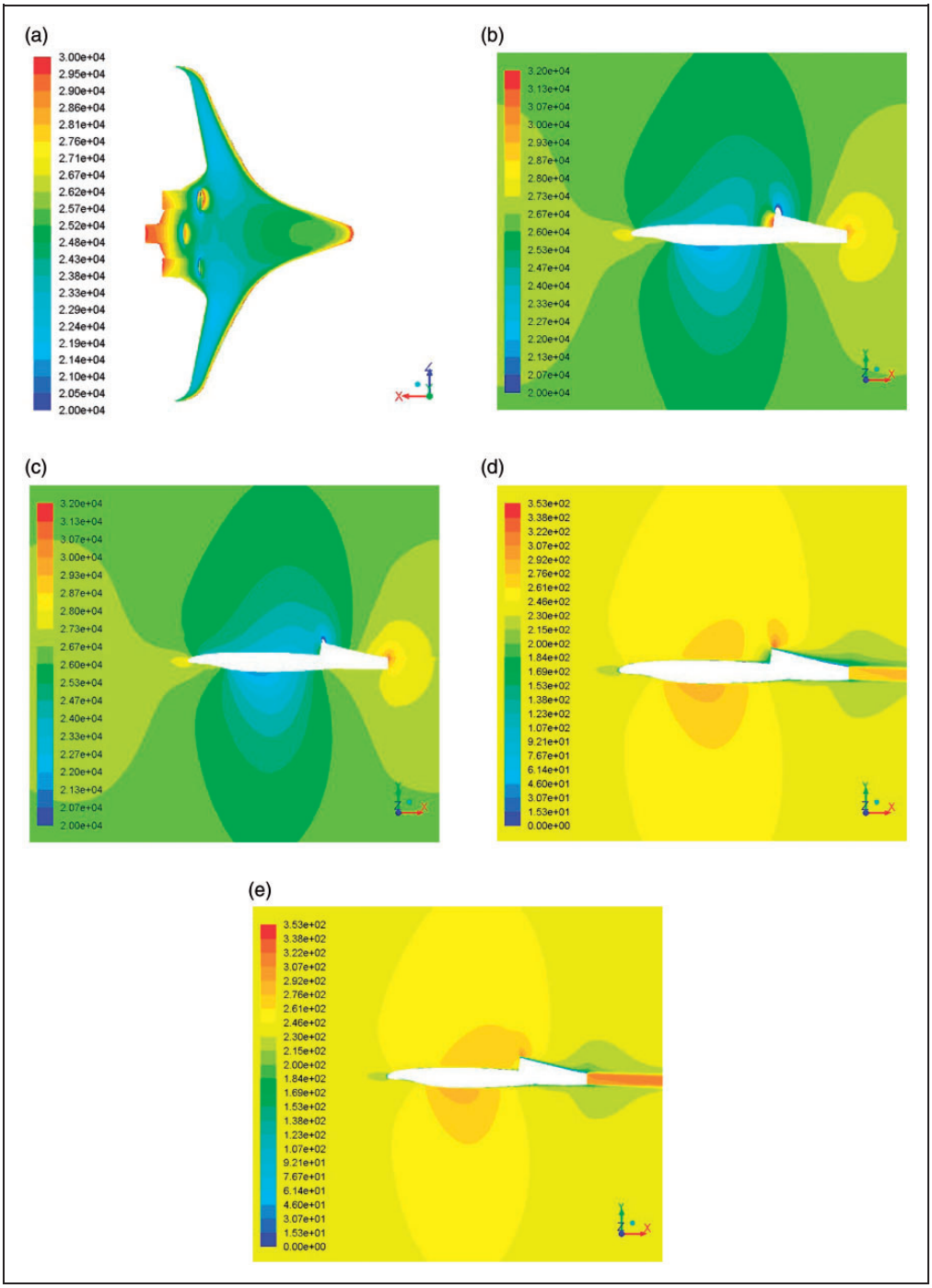

Figure 7. Velocity and pressure plots of $h = 10{,}000$ m, $Ma = 0.8$: (a) pressure plot, (Pa), $\eta_{BLI\_left} = 0.97$,$\eta_{BLI\_right} = 1.18$; (b) sectional pressure plot on left engine (Pa); (c) sectional pressure plot on right engine (Pa); (d) sectional velocity plot on left engine (m/s); (e) sectional velocity plot on right engine (m/s).

distributed engines are shown in Figure 5. And the corresponding roll and yaw moment coefficients C_M with $\eta_{BLI\_left} = 0.97$, $\eta_{BLI\_right} \in [0.97, 1.18]$ are calculated and shown in Figure 6.

As can be seen, the different BLI effects can significantly affect the lateral-directional aerodynamic characteristics. While the BLI intensity of the right engine is increasing, the differences in the lift, drag coefficients of the two wings ΔC_L, ΔC_D generally increase. And correspondingly, the negative rolling and yawing moments are generated due to the asymmetric aerodynamic lift and drag. The roll moment coefficient with $\eta_{BLI\_right} \in [0.97, 1.18]$ usually has an apparent change, and the variation range induced by differentiated BLI effects is from -0.0012 to 0. In comparison, the yaw moment coefficient varies just to a relatively small extent with the increasing BLI differences, and this reveals that the negative roll moment is the main factor in the lateral-directional aerodynamics induced by the differentiated BLI intensities. In summary, these results demonstrate that differentiated BLI intensities on

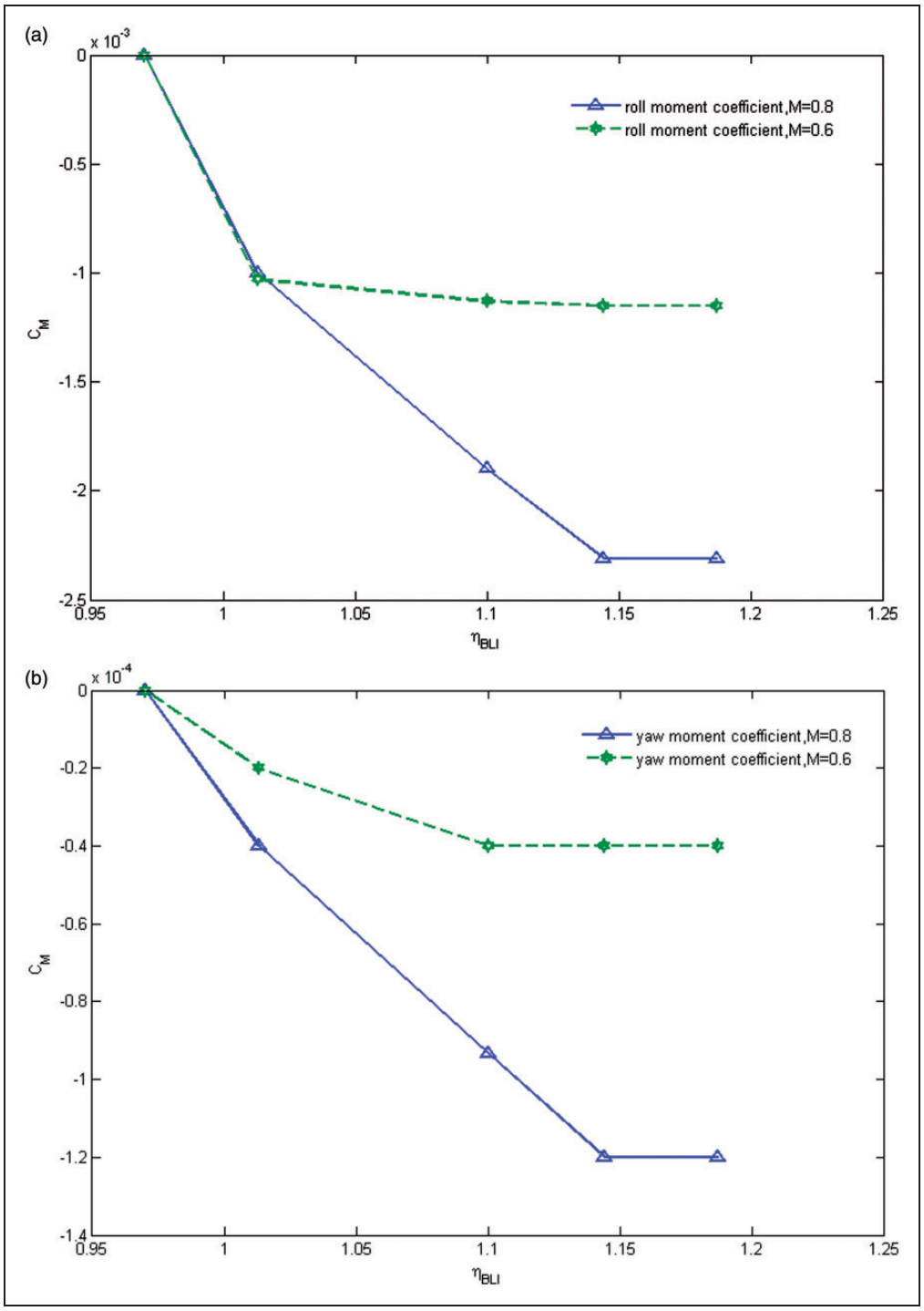

Figure 8. Comparisons of (a) roll and (b) yaw moment coefficients.

the distributed engines can certainly affect the lateral-directional aerodynamic characteristics of the DPC aircraft, and the change regularity of the aerodynamic roll and yaw moment coefficients due to BLI provides a reference for other DPC aircraft.

Furthermore, in order to compare the BLI influence between different velocities, another flight state $h = 10{,}000$ m, $Ma = 0.8$ is selected. With different BLI intensities $\eta_{BLI\_left} = 0.97$, $\eta_{BLI\_right} = 1.18$ on the left and right engines respectively, the velocity and pressure plots of the DPC aircraft are shown in Figure 7.

Accordingly, comparisons of the BLI influences on the aerodynamic roll and yaw moment coefficients C_M for different flight velocities $M = 0.6$ and $M = 0.8$ are shown in Figure 8.

Similar to the flight states $h = 10{,}000$ m, $Ma = 0.6$, the asymmetric velocity and pressure distribution of the DPC aircraft at higher velocity $M = 0.8$ are also distinctly appeared with the differentiated BLI intensities, as shown in Figure 7. Comparisons between the plots of the left and right engines show that a low-speed turbulence region occurs near the left nacelle with the smaller BLI intensity $\eta_{BLI\_left} = 0.97$, meaning that the flow field on the upper surface may be partly contaminated by this turbulence region. However, as the BLI intensity of the right engine increases to 1.18, the turbulence region near the right nacelle disappears, and the airflow in front of the engine inlet observably accelerates. Because of the asymmetric velocity and pressure characteristics, the aerodynamic roll and yaw moments are certainly generated.

Comparisons of the two aerodynamic moment coefficients illustrations in Figure 8 indicate that the variation range of the roll and yaw moment coefficients induced by the differentiated BLI effects is generally larger at higher velocity, which indicates that the influence of BLI on the lateral-directional aerodynamics tends to be relatively enhanced. For the roll moment coefficient, it will vary monotonously along with the intensifying BLI difference, and the maximum variation range is up to 0.0023 approximately. Similarly, the variation of the yaw moment coefficient related to BLI apparently presents a three-fold increase at $M = 0.8$. Generally, the BLI influences on the roll and yaw aerodynamic performance would be strengthened when the flight velocity increases.

In conclusion, all the results demonstrate that the differentiated BLI effects on the distributed engines can definitely affect the lateral-directional aerodynamic characteristics of the DPC aircraft. The change regularities illustrate that the influences of BLI on the aerodynamic roll and yaw moment coefficients appear to be enhanced along with the increasing BLI differences and flight velocity. These acquired regularities have certain reference value to other similar aircrafts. By effectively utilizing this unique lateral-directional aero-propulsive coupling effect, integrated flight/propulsion optimal control of the DPC aircraft can be achieved precisely.

Conclusion

The unique lateral-directional aero-propulsive coupling effect is an important feature of the DPC aircraft. Aiming at this point, this article conducts a preliminary study on this particular lateral-directional aerodynamic characteristic due to BLI. First, a general model-based 3D computational method is proposed to analyze the aero-propulsive coupling by the CFD computations. The determination of the essential boundary conditions is described in detail according to the thermodynamic DPS model. Then, a systematic analysis of BLI effects on the lateral-directional aerodynamic characteristics is carried out. The computational results demonstrate that differentiated BLI effects on the distributed engines can generate the aerodynamic roll and yaw moments evidently. The valuable regularities of the computation results under different BLI effects and flight states are concluded. The proposed method and common regularities are especially useful for other DPC aircraft. A point to be taken into further consideration is to achieve the integrated flight/propulsion control of this type of aircraft by taking advantage of the aero-propulsive coupling effect.

Acknowledgements

Authors acknowledge the research object derived from the Silent Aircraft Initiative program conducted by Cambridge University and MIT.

Declaration of Conflicting Interests

The author(s) declared no potential conflicts of interest with respect to the research, authorship, and/or publication of this article.

Funding

The author(s) disclosed receipt of the following financial support for the research, authorship, and/or publication of this article: This work was supported by the National Natural Science Foundation of China (Grant No.61304030) and China Scholarship Council.

References

1. Dangelo MM. *N+3 small commercial efficient and quiet transportation for year 2030–2035*. Report no. NASA/CR-2010-216691, US, 2010.
2. Mody PC, Sato S, Hall DK, et al. Conceptual design of an N+3 hybrid wing body subsonic transport. In: *The 28th AIAA applied aerodynamics conference*, Chicago, IL, USA, 28 June to 1 July 2010, AIAA paper 2010-4812.
3. Liebeck RH. Design of the blended wing body subsonic transport. *J Aircraft* 2004; 41: 10–25.
4. Hileman JI, Spakovszky ZS and Drela M. Airframe design for "Silent Aircraft". In: *The 45th AIAA aerospace sciences meeting and exhibit, special session: towards a silent aircraft*, Reno, NV, USA, 8–11 January 2007, AIAA paper 2007-453.

5. Hileman JI, Spakovszky ZS, Drela M, et al. Aerodynamic and aeroacoustic three-dimensional design for a "Silent" aircraft. In: *The 44th AIAA aerospace sciences meeting and exhibit*, Reno, NV, USA, 9–12 January 2006, AIAA paper 2006-241.
6. Hileman JI, Spakovszky ZS, Drela M, et al. Airframe design for silent fuel-efficient aircraft. *J Aircraft* 2010; 47: 956–969.
7. Elmiligui AA, Fredericks WJ, Guynn MD, et al. Numerical investigation of a fuselage boundary layer ingestion propulsion concept. In: *Aviation technology, integration, and operations conference*, Los Angeles, CA, USA, 12–14 August 2013, AIAA paper 2013-4402.
8. Kok HJ, Voskuijl M and Tooren MJ. Distributed propulsion featuring boundary layer ingestion engines for the blended wing body subsonic transport. In: *The 51st AIAA/ASME/ASCE/AHS/ASC structures, structural dynamics and materials conference*, Orlando, FL, USA, 12–15 April 2010, AIAA paper 2010-3064.
9. Atinault O, Carrier G, Grenon R, et al. Numerical and experimental aerodynamic investigations of boundary layer ingestion for improving propulsion efficiency of future air transport. In: *The 31st AIAA applied aerodynamics conference*, San Diego, CA, USA, 24–27 June 2013, AIAA paper 2013-2406.
10. Felder JL, Kim HD, Brown GV, et al. An examination of the effect of boundary layer ingestion on turboelectric distributed propulsion systems. In: *The 49th AIAA aerospace sciences meeting including the new horizons forum and aerospace exposition*, Orlando, FL, USA, 4–7 January 2011, AIAA paper 2011-300.
11. Plas A. *Performance of a boundary layer ingesting propulsion system*. Master Thesis, Massachusetts Institute of Technology, USA, 2006.
12. Plas AP, Sargeant MA, Madani V, et al. Performance of a boundary layer ingesting propulsion system. In: *The 45th AIAA aerospace sciences meeting and exhibit*, Reno, NV, USA, 8–11 January 2007, AIAA paper 2007-450.
13. Stoll AM, Bevirt JB, Moore MD, et al. Drag reduction through distributed electric propulsion. In: *The 2014 Aviation technology, integration, and operations conference*, Atlanta, GA, USA, 16–20 June 2014, AIAA paper 2014-2851.
14. Ochs SS, Tillman G, Joo J, et al. CFD-based analysis of a boundary layer ingesting propulsion. In: *The 51st AIAA/SAE/ASEE joint propulsion conference*, Orlando, FL, USA, 27–29 July 2015, AIAA paper 2015-3800.
15. Kim H, and Liou MS. Flow simulation of N2B hybrid wing body configuration. In: *The 50th AIAA aerospace sciences meeting including the new horizons forum and aerospace exposition*, Nashville, TN, USA, 9–12 January 2012, AIAA paper 2012-0838.
16. Lugo VM, Doulgeris G and Singh R. Computational analysis of the effects of a boundary layer ingesting propulsion system in transonic flow. *Proc IMechE, Part G: J Aerospace Engineering* 2012; 227: 1215–1232.
17. Kerho M. Aero-propulsive coupling of an embedded, distributed propulsion system. In: *The 33rd AIAA applied aerodynamics conference*, Dallas, TX, USA, 22–26 June 2015, AIAA paper 2015-3162.
18. Wick AT, Hooker JR and Hardin CJ. Integrated aerodynamic benefits of distributed propulsion. In: *The 53rd AIAA aerospace sciences meeting*, Kissimmee, FL, USA, 5–9 January 2015, AIAA paper 2015-1500.
19. Kang WW, Zhang J and Yang LY. Research on boundary layer ingestion effects of distributed propulsion configuration. In: *The 2014 IEEE Chinese guidance, navigation & control conference*, Yantai, China, 8–10 August 2014.
20. Blanco ER, Hall CA and Crichton D. Challenges in the silent aircraft engine design. In: *The 45th AIAA aerospace sciences meeting and exhibit*, *special session: towards a silent aircraft*, Reno, NV, 8–11 January 2007, AIAA paper 2007-454.
21. Ge H. *Research on modeling technology for high bypass ratio turbofan engine*. Master Thesis, Nanjing University of Aeronautics and Astronautics, China, 2013.

Appendix

Notation

A	cross-sectional area
C_L	lift coefficient
C_D	drag coefficient
C_M	moment coefficient
h	flight altitude
K	flow coefficient
M	Mach number
P	static pressure
P^*	total pressure
q_m	air flow rate
R	gas constant
T	static temperature
T^*	total temperature
V	velocity
η	efficiency coefficient
η_{BLI}	BLI intensity
γ	specific heat ratio
λ	velocity coefficient
π	pressure ratio
σ	total pressure recovery coefficient